IEEE Access
Multidisciplinary | Rapid Review | Open Access Journal

Received 26 June 2023, accepted 14 July 2023, date of publication 21 July 2023, date of current version 1 August 2023.

Digital Object Identifier 10.1109/ACCESS.2023.3297974

RESEARCH ARTICLE

Array-Beamspace Mapping for Planar Two-Dimensional Beam-Forming

WILLIAM L. BEARDELL[1], (Student Member, IEEE), JANUSZ MURAKOWSKI[2], GARRETT J. SCHNEIDER[2,3], AND DENNIS W. PRATHER[2,3], (Fellow, IEEE)

[1]Sensor Technologies Group, The Johns Hopkins University Applied Physics Laboratory, Laurel, MD 20723, USA
[2]Phase Sensitive Innovations Inc., Newark, DE 19713, USA
[3]Department of Electrical and Computer Engineering, University of Delaware, Newark, DE 19716, USA

Corresponding author: William L. Beardell (beardell@udel.edu)

This work was supported in part by the Air Force Research Laboratory under Contract FA8750-18-C-0182, and in part by the Air Force Office of Scientific Research under Contract FA9550-20-1-0301.

ABSTRACT As sixth-generation (6G) communication systems manifest at carrier frequencies well into the millimeter-wave (mmW) spectrum, the ability of conventional digital beamforming techniques to handle the beam-bandwidth product is increasingly stressed. Microwave photonic beamforming has been presented as a solution to this problem by up-converting a sampled RF field distribution to an optical carrier for analog beam-space processing, but to date has relied upon fiber arrays with the same dimensionality as the RF array, i.e., a two-dimensional RF array requires a two-dimensional fiber array and a three-dimensional optical processor to perform the Fourier transform required for two-dimensional beamforming. To address this problem, we present an approach to photonic mmW beamforming wherein two-dimensional phase information is preserved through a one-dimensional Fourier transform leveraging grating lobes in the array response. This approach carries several benefits, primarily as an enabler for leveraging photonic integrated circuits for RF-photonic beamforming, carrying with it a footprint reduction of more than ten thousand times. Furthermore, beamforming efficiency is increased for sources near the limits of the RF field-of-view; improvements to throughput power in such cases are as much as double. Theory, simulations, and experimental results in the form of images and videos are presented to validate the approach for a nineteen-element hexagonally-distributed phased array.

INDEX TERMS Arrays, beamspace, Fourier transform, beamforming, mapping, RF photonics, AB mapping.

I. INTRODUCTION

Grating lobes are often regarded as the bane of phased-array antennas: for sub-optimally sampled arrays wasted energy, directional ambiguity, multipath loss, and gives rise to other deleterious effects arise that reduce overall performance [1], [2]. Substantial theoretical and experimental effort has been devoted to the design of arrays for the purposes of minimizing side and grating lobes in applications with constrained size, weight, power, or number of elements [3], [4], [5], [6]. The methods range from front-end techniques, such as element design and array geometry, to back-end digital signal processing. Whereas periodic arrays allow for orthogonal beamforming [7], [8], [9], aperiodic arrays possess irregular null patterns and weak extinction between beams [6], [10], [11], [12]. Periodic arrays additionally exhibit greater beam efficiency, measured as a ratio of power in the desired beam versus total power radiated by the array. Orthogonal spatial division maximizes power transmission into and extinction between multiple beams and is typically performed with a digital beamforming network, leveraging electronic integrated circuits at the cost of expensive and power-hungry analog-to-digital converters (ADCs) and a computationally complex inverse Fourier transform (IFT) to compute the beamspace of the waves incident upon the array [13], [14].

The associate editor coordinating the review of this manuscript and approving it for publication was Davide Comite.

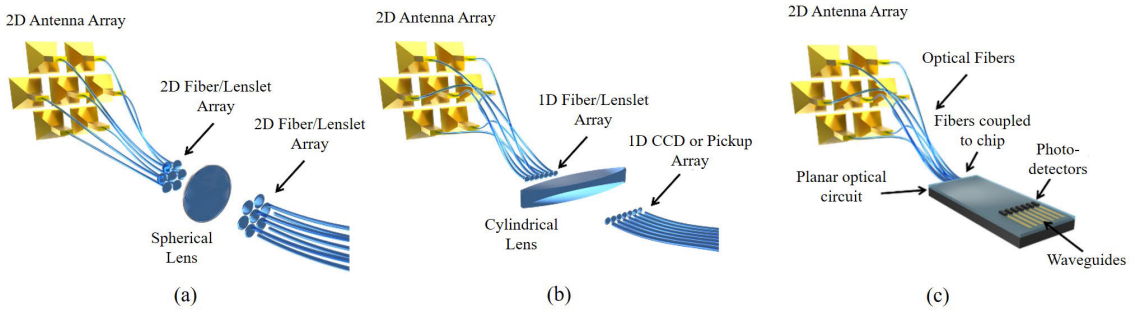

FIGURE 1. Conceptual illustration of two-dimensional beamforming using a two-dimensional (a) and one-dimensional (b) optical Fourier transform. The approach presented in this work enables planar optical processing on a photonic integrated circuit with no loss of information (c).

The burgeoning field of microwave photonics presents the opportunity to reduce beamforming cost, size, weight and power (C-SWaP) requirements by mixing the sampled RF field with an optical carrier through coherent up-conversion. Subsequent spatial processing can be carried out with free-space optical processing in the form of a lens [15], [16]. In prior work using this approach, the dimensionality of the optical Fourier transform has matched that of the antenna array: for two-dimensional beamforming, a two-dimensional Fourier transform must be performed (using a spherical lens as shown in Fig. 1(a)) upon an input field launched by a two-dimensional fiber array, with the result captured by a two-dimensional camera or fiber pickup array. In this case, the fiber launch array into the optical processor is arranged as a scaled replica of the RF array. If the RF array spacing falls on a periodic lattice, the optical point-spread function (PSF) exhibits periodicity as well, and a method of two-dimensional beamforming with a one-dimensional Fourier transform, as illustrated in Fig. 1(b), becomes possible: by harnessing grating lobes, linear (one-dimensional) steering of a single beam can generate all the resolved beams across a two-dimensional Fourier plane. This technique uncovers an abundance of further potential [17], especially the prospect of implementing two-dimensional beamforming within planar photonic integrated circuits (PICs) [18], as shown in Fig. 1(c).

In this work, we present an RF-photonic beamformer, in which two-dimensional RF scenes are processed with linear, i.e. one-dimensional, optical Fourier transforms with no loss of information.[1] The approach, which we term "Array-Beamspace (AB) Mapping," is illustrated for the case of one specific array, specifically a 19-element hexagonal array, with both simulations and an experimental demonstration. However, it is not limited to this one type of array, but rather can be applied generally to a wide class of arrays where the elements are distributed on a periodic lattice of either hexagonal or rectangular distributions [19]. The lattice herein takes a hexagonal distribution to approximate a circular aperture and take advantage of the denser packing of elements for a given horizontal baseline.

The remainder of this paper is structured as follows: Sec. II presents an overview of mmW imaging via coherent photonic up-conversion, while Sec. III presents a formulation of equivalent one- and two-dimensional beamspaces for the 19-element hexagonal array, and simulations to demonstrate the preservation of beam orthogonality in the two- to one-dimensional mapping. Sec. IV presents simulations of the operation of the experimental system with multiple incident RF sources and optical scan loss effects, and Sec. V presents the experimental setup and validation. Sec. VI discusses how these results may take further advantage of adjacent enabling technologies. Finally, Sec. VII contains a brief summary of the work.

II. OVERVIEW OF OPTICAL mmW IMAGING

A. SYSTEM ARCHITECTURE

The optical approach to millimeter-wave (mmW) beamforming begins with a conventional antenna array, with elements defining the RF band of interest, pitch defining the alias-free field-of-view (FOV) and aperture size defining the angular resolution. In the receive configuration, each antenna feeds a low-noise amplifier (LNA) driving an optical phase modulator, imposing the sampled RF field upon an optical carrier. A patented approach [20] preserves the coherence of the upconverted field by actively compensating for phase perturbations due to thermo-mechanical interference affecting each fiber. The modulators' output optical fibers are arranged into a fiber bundle that launches a scaled version of the RF phase front into a free-space optical processor where each fiber beam is collimated by a microlens; the waists of these beams are then placed in the front focal plane of a converging lens, with the Fourier transform of the input field located at the back [21]. An illustration of the optical processor configuration is shown in Fig. 2, while a detail of the two-dimensional antenna array is shown in Fig. 3. The horizontal spacing of 7 cm and vertical spacing of 6.1 cm results in an operational FOV of 7.4 degrees at 33 GHz, while the array's widest extent of 5 elements in the horizontal direction results in a resolution of 1.5 degrees at the same frequency.

[1] Rigorous proof that information is preserved is beyond the scope of this work and will be provided in a separate article currently in production [19].

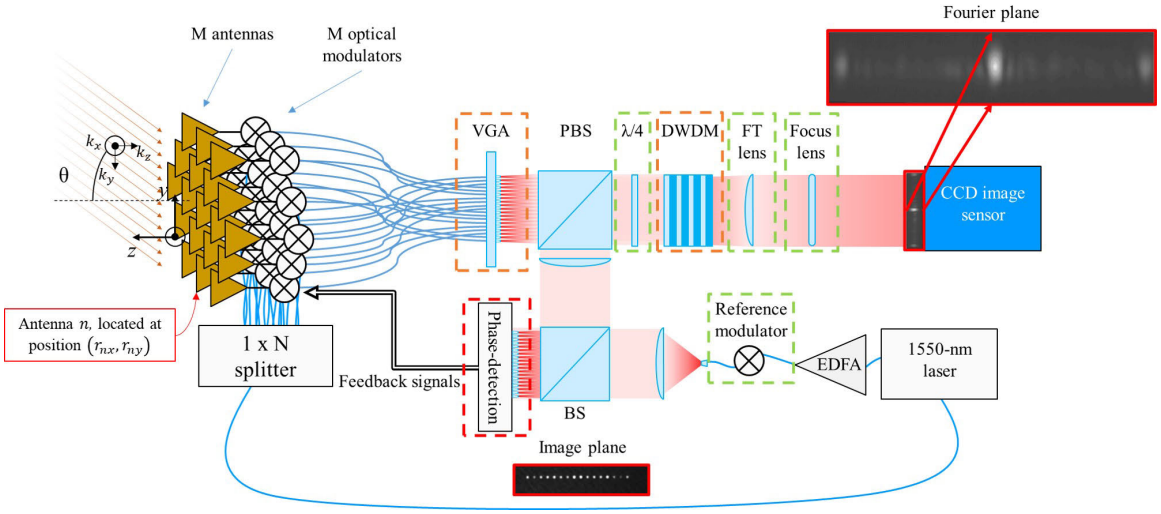

FIGURE 2. Not-to-scale Illustration of free-space optical processor including 19-element hexagonally-spaced antenna array feeding V-groove array (VGA) through array-beamspace mapping (AB Mapping). Antennas capture incident RF signals which drive optical modulators. Up-converted optical sidebands are filtered from carrier with dense wavelength division multiplexing (DWDM) filters. Optical Fourier transform performed by plano-convex cylindrical lens with curvature along axis of VGA distribution (FT lens) and transverse optical image focused by plano-convex lens oriented with curvature orthogonal to VGA axis and with focal length half of FT lens. Note that in reality FT and focus lenses are positioned as close as possible to each other along optical axis. Quarter-wave plate ($\lambda/4$) and polarizing beam-splitter (PBS) reflect optical carrier towards reference arm for phase locking. Reference modulator fed by linear phase sweep overlaid on optical image plane produces beat signals used by field-programmable gate array (FPGA, not depicted) to lock optical phase, preserving coherence of sampled RF field. Erbium-Doped Fiber Amplifier (EDFA) amplifies laser output for distribution to all antennas.

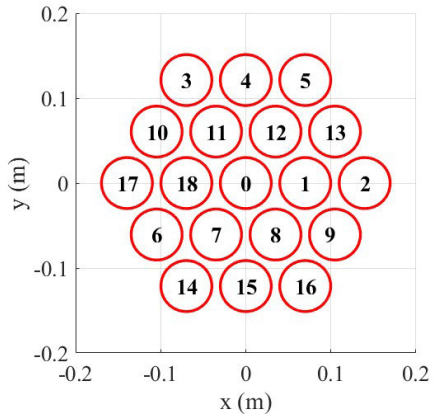

FIGURE 3. Frontal view of array geometry used in this work. 19-element hexagonal-baseline array with horizontal pitch of 7 cm and vertical pitch of 6.1 cm results in alias-free field-of-view (FOV) of 7.4 degrees and resolution of 1.5 degrees at 33 GHz.

B. OPTICAL mmW IMAGING

To process RF fields in an optical manner, we consider a system constructed similarly to the configuration shown in Figure 2: A plane wave impinges upon an array in the x-y plane, creating a phase distribution that depends upon the wave's angular frequency ω_{rf} and angles-of-arrival; that is, the wave creates a phase at the n^{th} element ϕ_n calculated through the dot product of the wave's k- vector

$$|\mathbf{k}| = \frac{\omega_{\text{rf}}}{c} = \frac{2\pi}{\lambda} \tag{1}$$

with the antenna positions $\mathbf{r}_n$ shown in Fig. 2:

$$\phi_n = \mathbf{k} \cdot \mathbf{r}_n = k_x r_{nx} + k_y r_{ny} \tag{2}$$

where the antennas are assumed to lie in the x-y plane.

Following spatial sampling by the distributed aperture, the electric field is amplified by an LNA before entering a lithium niobate phase modulator, wherein the phase of a C-band optical carrier of wavelength λ common to all elements is modulated in linear proportion to the strength of the applied electric field ultimately originating from the incident RF field. The result, when taken as the aggregate of all phase modulator outputs, is representative of the RF field incident upon the array. Following modulation, the field is passed through an array of optical fibers that, for the purpose of this work, are of equal length. After fiber propagation, for two-dimensional optical imaging the fibers are coupled to a fiber array representing a scaled version of the RF array: i.e. the upper right antenna and modulator feeds the upper right fiber, the upper left antenna feeds the upper left fiber, and so on. In the case of AB mapping, the i^{th} fiber is connected to the n^{th} antenna; the association between antenna and VGA position will be elucidated in Sec. III. In either case, the pitch of the optical array is several hundred times smaller than the pitch of the RF array, and is noted herein by the factor s. A microlens array is placed in front of the fiber array such that each microlens sits in front of each fiber facet. This step allows for highly collimated light of waist σ to enter the free-space optical system, improving efficiency and reducing stray light when compared with the highly divergent optical field launched from a plain fiber facet.

For the purpose of this work, linear microlens arrays in fused silica have been supplied by Suss MicroOptics, S.A. with element pitch of 250 μm and radius of curvature of 422 μm. These specifications have been chosen primarily due to the availability of such devices and the favorable characteristics of the field distribution launched by this configuration. Following launch into the optical processor, a series of dense wavelength division multiplexing (DWDM) filters remove the optical carrier from the sideband, allowing the restriction of Fourier-plane analysis to the upper sideband. In addition, the use of polarization-maintaining fiber throughout the system allows for the assumption of co-polarization, further simplifying analysis.

Considering only the sideband, the launched field A_i from the i^{th} fiber located at horizontal VGA position x_i into the optical processor takes the form

$$A_i(x, y) = \frac{1}{\sqrt{\pi}\sigma} \exp\left[-\frac{(x - x_i)^2 + y^2}{2\sigma^2}\right] \exp\left[-j\phi_n\right] \quad (3)$$

assuming the VGA is distributed along the x axis of the input focal plane. The association of i and n allows the phase of the n^{th} antenna to be expressed as the phase ϕ_i of the i^{th} fiber. The launched optical field is then the superposition of all i fields:

$$A(x, y) = \sum_{i=1}^{N} A_i(x, y). \quad (4)$$

Placing the launched field in the front focal plane of a plano-convex cylindrical lens of focal length f with curvature oriented along the axis of fiber distribution (that is, horizontally) results in an optical field at the back focal plane of this lens representing the one-dimensional analog Fourier transform of the input field A. Directly behind the lens of focal length f along the optical path lies a plano-convex lens of focal length $f/2$ with curvature oriented transverse to the axis of distribution (vertically), resulting in direct imaging of the vertical field distribution at the back focal plane. Thus, the one-dimensional Fourier transform $A_i(u, v)$ of the i^{th} input field takes the form

$$A_i(u, v) = \frac{2\sigma\sqrt{\pi}}{f\lambda} \exp\left[-j\left(\phi_i + \frac{2\pi}{f\lambda} x_i u\right)\right] \times \exp\left[-2u^2\left(\frac{\pi\sigma}{f\lambda}\right)^2\right] \exp\left[-\frac{v^2}{2\sigma^2}\right] \quad (5)$$

with the total field again following the superposition:

$$A(u, v) = \sum_{i=1}^{N} A_i(u, v). \quad (6)$$

For a constant VGA spacing $|x_i - x_{i+1}|$ and operational restrictions on wavelength λ generally dictated by available DWDM and other components, there remain independent variables in Equation (5) that may be manipulated to create a field at the Fourier plane with the desired characteristics, such as the input waist σ and focal length f. Such analysis is outside the scope of this work, and values of $\sigma \approx 60$ μm and $f = 100$ mm have been identified as suitable herein for proof of the relevant concepts. Further analysis is presented in [22], [23], and [24].

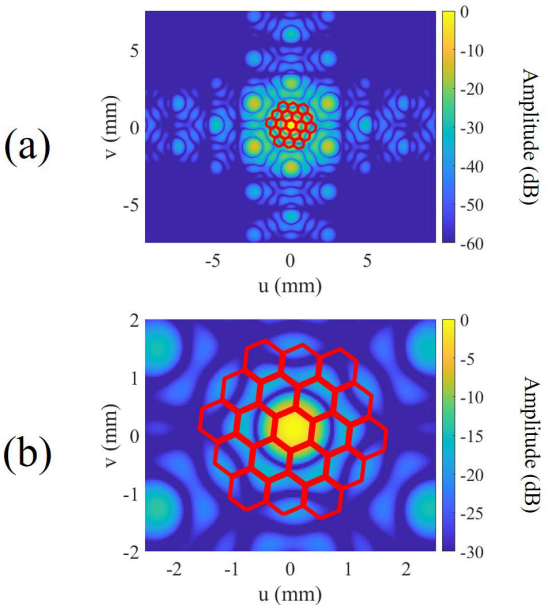

FIGURE 4. (a) Log-scale PSF with tiled beamspace for a 19-element hexagonal array. All unique information is contained within the red beamspace array in the center; repetition occurs in tessellated pattern in all directions. Each red bin indicates one of the 19 resolved beams. (b) Detail of the beamspace array showing orthogonal beam division. Maximum inside one beam center results in null in all other beam centers within the beamspace array.

Equations (5) and (6) represent closed-form expressions for an optical field steered with phases ϕ_n processed by a one-dimensional Fourier transform and imaged in the transverse axis. The following analysis will motivate and elucidate the relation between the n^{th} antenna and the i^{th} fiber.

C. GRATING LOBES

As discussed in Sec. II-A, the RF figures of merit of the photonic mmW beamformer are wholly determined by the antenna spacing and aperture size. For optical beamforming, a scaled version of the RF array is constructed from optical fibers with a one-to-one position correspondence: antenna positions map to fiber positions for relaunch of the RF field placed upon an optical carrier. As a result, the beamspace of the optical array is fundamentally similar to the beamspace of its RF counterpart: if the RF array is periodic, so too is the optical array. If two (or more) plane waves impinge upon the RF array with orthogonal phase distributions, the corresponding optical beamspace will exhibit maximal modal separation between spots in the Fourier plane corresponding to the **k**-vectors representative of the impinging phase distribution [19]. Fig. 4(a) depicts the point-spread function (PSF) of a 19-element hexagonal array.

Note in Fig. 4(a) the presence of grating lobes: the periodically tiled pattern of maximal energy represents copies of the information contained in the red-highlighted region

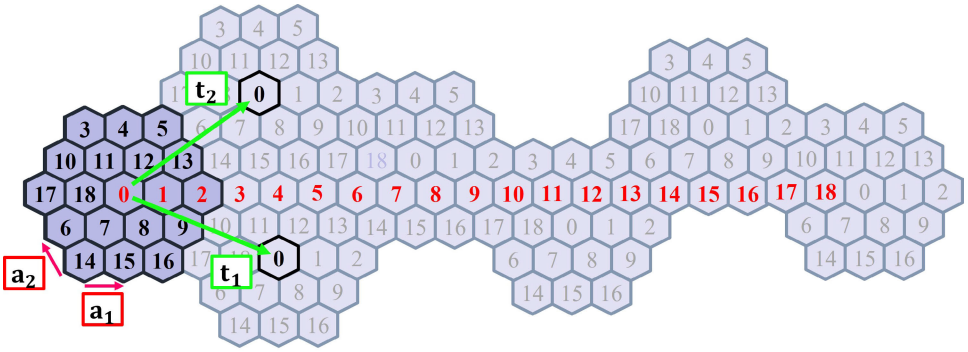

FIGURE 5. Illustration of the antenna-element enumeration (left) and notional extension thereof, forming a linear array enumerated from 0 to 18. Tessellation-lattice basis vectors (t_1, t_2) allow the entire plane to be filled with the 19-element array.

in the center of the extended optical Fourier plane [25]. If a beam is steered along any direction past the point where the main lobe leaves the center region, a grating lobe will enter at the same time. Therefore, if a beam may be steered along a straight line and have either the main or grating lobe visit each division of this center region, the one-dimensional optical beamspace can be considered representative of the associated two-dimensional RF beamspace.

Further, shown in Fig. 4(b) is the property of orthogonal spatial division: when a beam is aligned to the center of one one 'bin' on the Fourier plane, there is a null centered in all other bins. As a result, two beams falling into separate bins may have the same carrier frequency; coupling between bins is minimized for these cases, enabling frequency reuse. We shall see that this property of beam orthogonality is preserved in the beamspace mapping from two dimensions to one.

At this stage, we have considered a 19-element hexagonal array capable of orthogonal spatial multiplexing and with the potential for linear beamsteering to visit all resolvable beams in two dimensions. As the beam is steered along any given direction, the associated grating lobes will of course translate along the same direction. As the beam reaches the edge of the beamspace array, a grating lobe will enter to replace it, such that there is always a 'main' lobe inside the central portion of the Fourier plane, highlighted in red in Fig. 4(a). For example, the broadside beam is continually steered along an axis parallel to the direction between the broadside bin and any neighbor, the 'main' lobe visits each bin once and only once before returning to the broadside bin [19]. As a result, **any two-dimensional phase front may be represented by an equivalent one-dimensional phase distribution, and, by extension, may be equivalently beamformed by a one-dimensional Fourier transform.**

III. PLANAR TWO-DIMENSIONAL BEAMFORMING

A. ARRAY SPACE VECTORS

To identify the relationship between the two-dimensional antenna array, the one-dimensional fiber array, and the resulting one- and two-dimensional beamspaces, consider the antenna enumeration shown in Fig. 5. The triangular lattice basis is

$$\mathbf{a}_1 = \begin{pmatrix} 1 \\ 0 \end{pmatrix} \quad \mathbf{a}_2 = \frac{1}{2}\begin{pmatrix} -1 \\ \sqrt{3} \end{pmatrix}. \tag{7}$$

The tessellation basis vectors $\mathbf{t}_1$ and $\mathbf{t}_2$ then define the location of corresponding elements in notional neighboring periodic arrays. As shown in Fig. 5, for a 19-element array, the tessellation basis vectors may be chosen as

$$\mathbf{t}_1 = \begin{pmatrix} 4 \\ -\sqrt{3} \end{pmatrix} = 3\mathbf{a}_1 - 2\mathbf{a}_2 \tag{8a}$$

$$\mathbf{t}_2 = \frac{1}{2}\begin{pmatrix} 7 \\ 3\sqrt{3} \end{pmatrix} = 5\mathbf{a}_1 + 3\mathbf{a}_2. \tag{8b}$$

The tessellation matrix $\mathbf{T}$ is defined as the transposition of the above coefficients in relation to $\mathbf{a}_1$ and $\mathbf{a}_2$:

$$\mathbf{T} = \begin{pmatrix} 3 & 5 \\ -2 & 3 \end{pmatrix} = \begin{pmatrix} T_{11} & T_{12} \\ T_{21} & T_{22} \end{pmatrix}. \tag{9}$$

Note that $\det(\mathbf{T})$ equals the number of elements in the array, and by extension the number of independently resolvable beams [19].

The specific choice of enumeration and determination of the basis vectors $(\mathbf{a}_1, \mathbf{a}_2)$ and $(\mathbf{t}_1, \mathbf{t}_2)$ used here is not unique—as long as the extended element space may be filled without gaps or duplicate positions, any choice of vectors is suitable, provided a linear progression of all element numbers is created. With reference to Fig. 5, it is clear that if the elements are phased according to the indicated enumeration, the result is equivalent to steering across the unambiguous field-of-view for the notional one-dimensional array indicated by red numeric labels.

A phase front impinging upon the antenna array induces a *virtual beam* in the elements as determined by the antenna positions and the $\mathbf{k}$-space composition of the incident wave: a virtual beam is hence defined as a 19-element vector comprising the complex amplitude of the impinging field as sampled by each array element [19]. Adding integer multiples of 2π to the phase of any element does not change this virtual beam.

As a result, we may fold the notional elements extending in a straight line back into their positions in the original array, mapping the notional one-dimensional array onto the physical/actual two-dimensional array. Or in the case of a two-dimensional array, add multiples of 2π to each phase correspondent to extending the elements along the line from 0 to 18 shown in Fig. 5, mapping the two-dimensional array onto the one-dimensional. Utilizing this scheme, we may enumerate equivalent beamspace arrays with elements distributed along either one or two dimensions. For the m^{th} virtual beam, the phase ϕ_n of the n^{th} element of an N-element array (either one- or two-dimensional) is given by

$$\phi_n = \frac{2\pi mn}{N}. \tag{10}$$

Here we again note the association between the i^{th} fiber and the n^{th} antenna; i.e. the phase of the i^{th} fiber corresponds to the phase of the n^{th} antenna.

B. BEAMSPACE VECTORS

By applying the phases calculated through (10), beams occupying each bin in one- and two-dimensional space may be generated that are also orthogonal to all other beams created in this manner. It is through this relation that the corresponding enumerations of both beamspaces shown in Fig. 6 are determined; by appplying these phases to the front-end channels, a broadside source may be steered into each of the 19 resolvable orthogonal beams shown in the upper portion of Fig. 6 as well as the equivalent one-dimensional beamspace in the lower portion of the Figure. Note that the two-dimensional beamspace has a slight rotation: this proceeds from the definition of the beamspace lattice basis vectors $\hat{\mathbf{t}}_1$, $\hat{\mathbf{t}}_2$ shown in Fig. 6 as presented below.

The element space and the beamspace are reciprocal spaces, with conversion between them accomplished by Fourier transformation. The beamspace-lattice basis vectors are therefore related to the tessellation basis vectors according to

$$\hat{\mathbf{t}}_i \cdot \mathbf{t}_j = 2\pi\delta_{ij}, \;\; i,j \in \{1,2\} \tag{11}$$

where δ_{ij} is the Kronecker delta. Note that since the choice of lattice basis $\{\mathbf{a}_1, \mathbf{a}_2\}$ and tessellation basis $\{\mathbf{t}_1, \mathbf{t}_2\}$, is non-unique, then neither is the resultant beamspace basis $\{\hat{\mathbf{t}}_1, \hat{\mathbf{t}}_2\}$ and grating-lobe basis $\{\hat{\mathbf{a}}_1, \hat{\mathbf{a}}_2\}$. However, the latter bases depend upon the specific choice of the former. Vectors $\hat{\mathbf{t}}_1$ and $\hat{\mathbf{t}}_2$ are found using the property (11) by first constructing a matrix $\mathbf{B_t}$ from column vectors (8)

$$\mathbf{B_t} = \begin{pmatrix} 4 & \frac{7}{2} \\ -\sqrt{3} & \frac{3\sqrt{3}}{2} \end{pmatrix}, \tag{12}$$

and then extracting the column vectors from matrix

$$\mathbf{B}_{\hat{\mathbf{t}}} = 2\pi\left[(\mathbf{B_t})^T\right]^{-1} = \frac{2\pi}{19}\begin{pmatrix} 3 & 2 \\ -\frac{7}{\sqrt{3}} & \frac{8}{\sqrt{3}} \end{pmatrix} \tag{13}$$

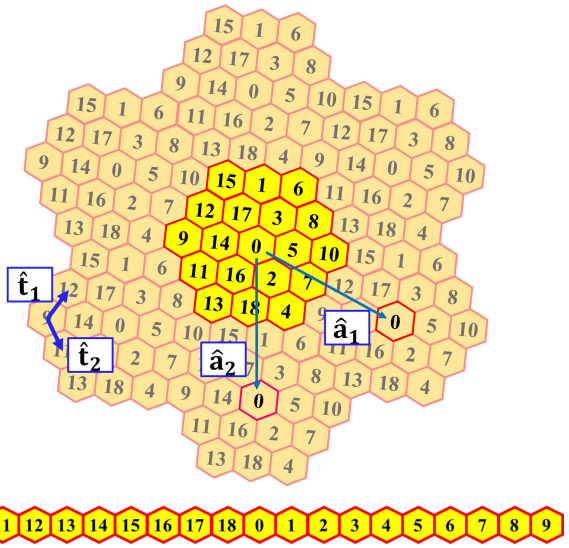

FIGURE 6. Top: Extended and enumerated two-dimensional beamspace lattice showing beamspace basis vectors ($\hat{\mathbf{t}}_1, \hat{\mathbf{t}}_2$) and grating-lobe basis vectors ($\hat{\mathbf{a}}_1, \hat{\mathbf{a}}_2$). Note that due to the imaging convention used herein, the vertical axis of the beamspace has been flipped. Bottom: Equivalent one-dimensional beamspace lattice with corresponding enumeration.

to yield the beamspace-lattice basis

$$\hat{\mathbf{t}}_1 = \frac{2\pi}{19}\begin{pmatrix} 3 \\ -\frac{7}{\sqrt{3}} \end{pmatrix}, \; \hat{\mathbf{t}}_2 = \frac{2\pi}{19}\begin{pmatrix} 2 \\ \frac{8}{\sqrt{3}} \end{pmatrix}. \tag{14}$$

Further, the lattice along which the grating lobes fall, or the grating-lobe lattice, may be determined with the coefficients of the tessellation lattice defined in (8). Since we have defined the tessellation lattice through integer multiples of the array basis, we may in the same way define the grating-lobe lattice through integer multiples of the beamspace lattice. Accordingly, the grating lobe lattice is obtained using the grating-lobe basis $(\hat{\mathbf{a}}_1, \hat{\mathbf{a}}_2)$ shown in Fig. 6 (with the vertical axis flipped to agree with imaging convention) and defined by relations

$$\hat{\mathbf{a}}_1 = T_{11}\hat{\mathbf{t}}_1 + T_{12}\hat{\mathbf{t}}_2 \tag{15a}$$

$$\hat{\mathbf{a}}_2 = T_{21}\hat{\mathbf{t}}_1 + T_{22}\hat{\mathbf{t}}_2. \tag{15b}$$

The vectors (15) define the beamspace lattice positions occupied by grating lobes when the main lobe falls in the center of the image plane, and the offset coordinates from any other beam to its corresponding grating lobe(s).

Equivalently, the grating-lobe basis $(\hat{\mathbf{a}}_1, \hat{\mathbf{a}}_2)$ may be obtained directly from the lattice basis $(\mathbf{a}_1, \mathbf{a}_2)$ using the following relation analogous to (11):

$$\hat{\mathbf{a}}_i \cdot \mathbf{a}_j = 2\pi\delta_{ij}, \;\; i,j \in \{1,2\}. \tag{16}$$

For beams generated through (10), one can see the orthogonality in both the two-dimensional and associated one-dimensional beamspaces in Fig. 7, which shows the two-dimensional PSF and associated one-dimensional line-spread function (LSF) for the same incident virtual beam.

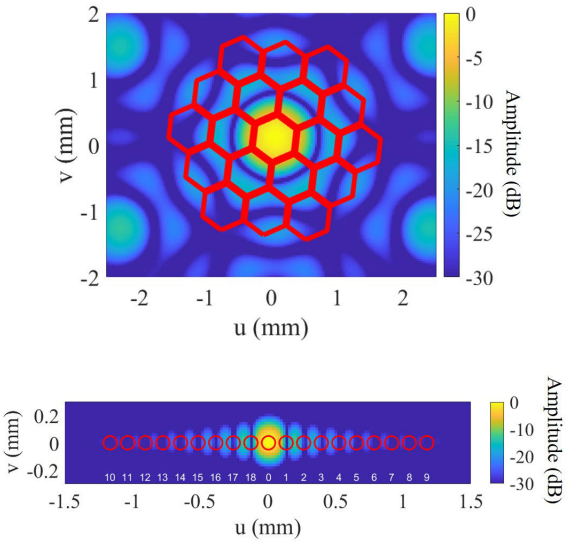

FIGURE 7. Simulated log-scale two-dimensional PSF (top, duplicated from Fig. 4(b)) and one-dimensional LSF (bottom) showing beam orthogonality in both transforms: maximum in one bin results in nulls in all other bins. Log-scale emphasizes orthogonality between beams.

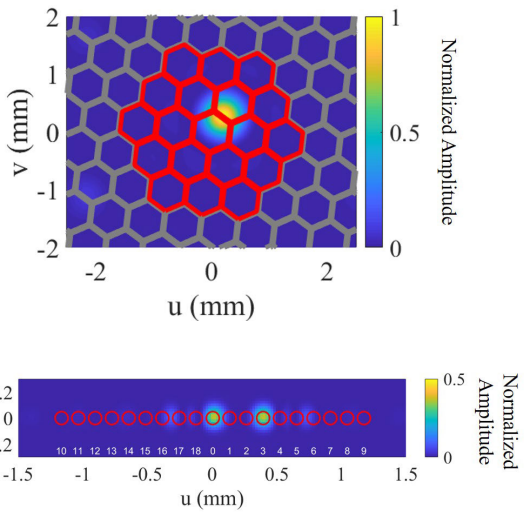

FIGURE 8. Simulated linear-scale point- (top) and line-spread (bottom) functions showing division of power between one-dimensional bins corresponding to the two beams across which an interstitial beam falls. Note in the one-dimensional beamspace that the peak power density is half of that in the two-dimensional beamspace since the beam is divided between beams 0 and 3.

Of course, a primary concern with any resampling technique is loss of information: The two-dimensional Fourier transform results in a two-dimensional beamspace wherein each discrete element of the beam lattice has 6 adjacent 'neighbor' beams, while in the beamspace from the one-dimensional FT, each beam has only 2 neighbors. From this observation it may seem that the mapping from two dimensions to one dimension must lose some information. In fact, however, for incidence cases in which a beam is split between adjacent bins (i.e., an interstitial beam), the resulting reconstructed two-dimensional beamspace *preserves* this information: if the two-dimensional beamspace is rebuilt by integrating the power in each one-dimensional bin, interstitial beams will be revealed as two beam bins dividing the total power of the incident beam, as shown in Fig. 8 for the case of an interstitial beam located between beams 0 and 3, as enumerated in Fig. 6—note that the power is divided appropriately even though the two bins are not adjacent in the one-dimensional beam array. If the number of elements (and therefore beams) is allowed to grow very large, this process is effectively convergent to a continuous two-dimensional FT despite being processed in only one spatial dimension.

At this stage, we have fully defined the coordinate system in which the antenna elements lie, as well as the beamspace coordinates, and a method for generating orthogonal virtual beams through phase distributions along one- and two-dimensional arrays. The association between the two coordinate spaces follows the Fourier transform relationship in which the 'large' coordinate in element-space corresponds to the 'small' coordinate in beamspace and vice versa: the grating lobe basis is reciprocal to the array basis, while the beamspace basis is reciprocal the tessellation basis, in accordance with (16) and (11), respectively.

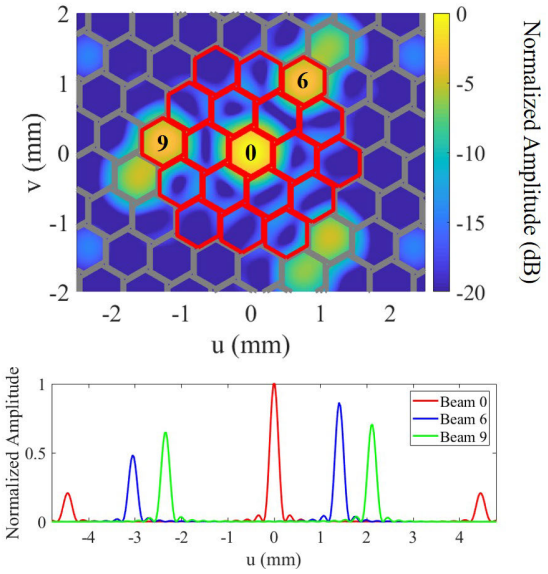

FIGURE 9. Illustration of combined incidence of beams 0, 6, and 9 in two (top) and one (bottom) dimensional beamspace. Orthogonality in two dimensions is preserved in the one-dimensional beamspace.

IV. SIMULATED OPERATION

A simulated example of three orthogonal beams (numbers 0, 6, and 9) incident at the same time in both one- and two-dimensional space is shown in Fig. 9. Note that each beam's maximum is aligned to nulls of the other beams in the one-dimensional plot, suggesting beam orthogonality, just as in the corresponding two-dimensional plot. The linescan response is simulated by drawing a horizontal line across the $v = 0$ axis of the one-dimensional beamspace and plotting the amplitude of each pixel along this line. This is later replicated in the presentation of experimental results.

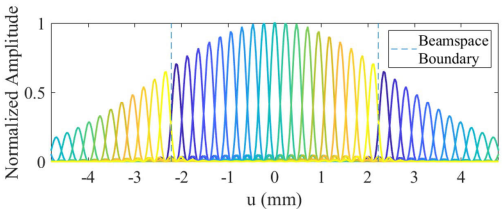

FIGURE 10. Linear plot showing all 19 orthogonal beams. Discontinuous color corresponds to boundaries between central beamspace array and grating-lobe neighboring regions of LSF. Integer values of beam number *m* correspond to color scale from blue to yellow, with phases applied to the two-dimensional front-end through Equation (10) scanning the main lobe across the linear field-of-view.

Overlaying all 19 orthogonal beams as shown in Fig. 10 illustrates the element factor of the launch assembly into the optical processor. Edge beams experience diminished optical power as the grating lobe grows stronger as it approaches the opposite edge of the one-dimensional beamspace; this phenomenon combined with the fact that these edge beams are the furthest extent from the center of the image plane results in diminished power captured from these outer beams. Planar beamforming optimizes the throughput to all beams; confining the spread of optical energy to the horizontal direction exclusively rather than both horizontal and vertical directions results in focused power and higher processing efficiency as defined by the ratio of energy in each beam to total energy at the Fourier plane [23]. In Fig. 10, each color in the plot represents beams generated by unique values of m from (10); the discontinuous color step near $|x| = 2$ mm represents the boundary between the fundamental beamspace and the grating lobe domain, i.e., all unique information is contained in the space between the boundaries shown, filling the alias-free field of view.

The comparison between the response in one and two dimensions makes plain an additional benefit of the resampling approach: For the linear edge case (beam 9), the optical scan loss is only 3 dB at the edge of the one-dimensional beamspace. The implication of this is twofold: first, only the RF scan loss in the horizontal direction (due to the antenna element factor) is incurred for the edge beam along the azimuth to combine with the 3-dB optical scan loss. Second, the two-dimensional corner-beam case in beam 6, which incurs RF scan loss both horizontally and vertically, is formed optically towards the center of the one-dimensional beamspace and incurs an accordingly minor penalty from the optical scan loss. An equivalent two-dimensional beamforming network in an optical implementation would incur dual scan-loss penalties for corner cases such as Beam 6 since element-factor roll-off is manifested in both (azimuthal and elevation) directions for both optical and RF element factors, while Beam 9 would incur roughly 3 dB of scan loss as a result of being only on the outside edge of the horizontal aperture.

An alternative way to understand this one-dimensional processing advantage is by considering that element-factor roll-off can be attributed to the sharing of power among the main lobe and nearby grating lobes. The edge beams in the two-dimensional beamspace lose power to the strengthening of 2-3 neighboring grating lobes; in contrast, in the one-dimensional beamspace the edge beam shares power with only 1 grating lobe, minimizing scan loss.

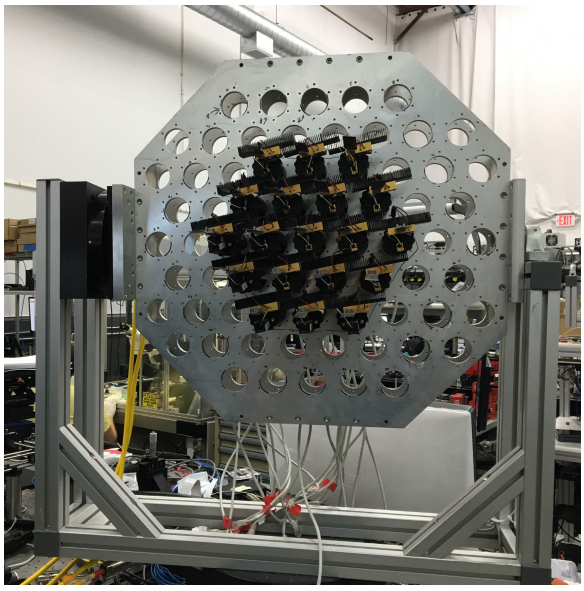

FIGURE 11. Assembled 19-element RF front-end with LTSA elements and RF-Lambda LNAs.

V. EXPERIMENTAL VALIDATION

A. SYSTEM ARCHITECTURE

Experimental validation proceeds with the construction of a 19-element antenna array distributed on a triangular lattice. For the purpose of this experiment, elements with sensitivity in the Ka-band from 26 to 40 GHz were used. Array elements are linear tapered slot antennas (LTSAs) with a 10° 3-dB beamwidth feeding RF-Lambda RLNA26G40GB low-noise amplifiers (LNAs) with an identical bandwidth. The assembled RF front-end is shown in Fig. 11. Optical up-conversion is accomplished with commercial off-the-shelf Covega 40-GHz phase modulators; these devices are also responsible for phase corrections enabling optical imaging of RF beams; as discussed in the following section, phase perturbations are measured and corrected through changing bias voltages applied to each modulator.

The free-space optical processor shown in Fig. 12 accomplishes two tasks: reimaging of the launched field with an overlaid reference for phase correction/locking, and Fourier transformation of the upper sideband of the launched field for mmW imaging [22]. While a detailed description of the former is outside of the scope of this work, briefly, the configuration consists of a $4f$ optical system relaying an unmagnified image of the launch array onto a photodetector array, with a reference beam overlaid upon the entire image with a swept phase, creating a distinct beat signal from each detector which is used to measure perturbations in the signal emanating from each fiber in real-time. These disturbances

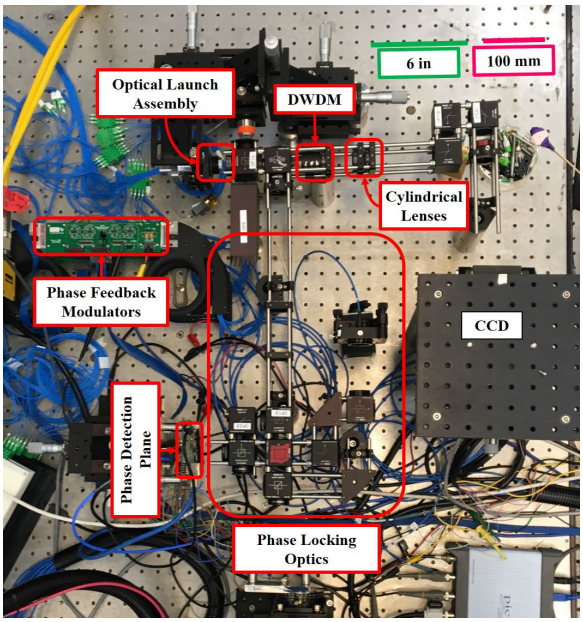

FIGURE 12. Setup of experimental optical processor with sideband imaging path across top and right-hand-side, and phase locking path at bottom left. Optical launch at top left consists of V-groove array coupled to microlens array for optimal launch profile. Optical carrier reflected off DWDMs passes back through beamsplitter and redirected to phase detection plane for active phase perturbation cancellation. Sidebands imaged in one dimension at CCD camera plane.

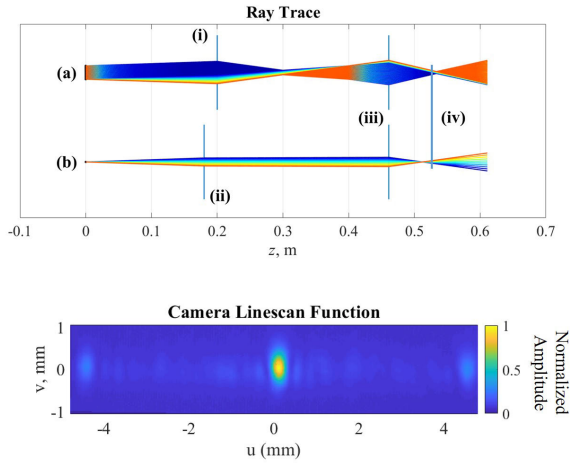

FIGURE 13. Top: Simplified ray trace showing optical beamforming network from above (a) and from side (b). Element (i): $f = 100$ mm cylindrical lens, (ii): $f = 200$ mm cylindrical lens, (iii): $f = 50$ mm spherical lens, (iv): CCD Camera location. Bottom: Experimental Fourier plane as sampled by CCD Camera. Linescan functions are taken from a horizontal line across the center of this image. Slight misalignment in convergence between horizontal and vertical seen in upper pane results in astigmatism manifested through elliptical main lobe on camera in lower pane.

are then inverted and applied at the upconversion module in an active manner. This phase-locked loop (PLL) enables faithful representation of the RF phase front at the input to the optical processor [20].

The second portion of the optical processor consists of optical band-pass filters to remove the optical carrier from the field propagated to the Fourier plane. For the one-dimensional launch configuration, in the direction along which the fibers are distributed in the launch array the processor represents a $2f$ system — the VGA is placed in the front focal plane of a cylindrical lens, and the resultant Fourier transform is found at the back focal plane. In the transverse direction a $4f$ system is realized with a cylindrical lens to relay the vertical image. This dictates that the focal length of the Fourier lens should be twice that of the transverse relay lens. For the purpose of this investigation, a focal length of 200 mm was chosen for the $2f$ system due to various constraints in the construction of the optical network. As a result, the transverse relay lens has a focal length of 100 mm. Finally, to optimize the spatial sampling of the Fourier plane by our Goldeye® G007 charge-coupled device (CCD) camera, a magnification factor of 4.5 times was applied using a spherical biconvex lens; the resulting Fourier plane contains the main lobe centered on the camera with grating lobes just at the edge of the CCD aperture. A simplified ray trace of the one-dimensional Fourier transforming optical system is shown from above (a) and from the side (b) in the upper portion of Fig. 13, while the two-dimensional camera image is shown in the lower portion of the same Figure. Cylindrical optical elements (i) and (ii) are plano-convex cylindrical lenses with refractive power aligned to the axis of interest, while optical element (iii) is a bi-convex spherical lens relaying the input image to the camera plane. Line-spread functions presented in the results and accompanying videos are obtained by drawing a horizontal line across the CCD image and obtaining pixel amplitudes along the line.

B. SOURCE SETUP

The source configuration for validation consists of various tone generators emitting continuous-wave (CW) 33-GHz signals that are radiated through one or multiple WiseWave ARH-2220-02 standard-gain horn antennas. These sources were placed a distance of approximately 4 meters from the array plane; for our RF wavelength of 9.1 mm, and array aperture of 280 mm this is suitably in the far-field for plane-wave incidence. A phase calibration was performed to compensate for unequal optical fiber path lengths from the front-end upconversion modulators to the free-space optical processor among the 19 array channels. This calibration was carried out by placing a single RF source broadside to the array, enabling the LNA for a single reference channel, and sequentially enabling each other channel one at a time, sweeping the phase of the other channel to center the maximum of each pairwise fringe pattern on the camera sensor.

C. RESULTS

Validation of the 19 orthogonal beams proceeded by applying the phases calculated through (10) to the antenna elements. The beam was then captured across the one-dimensional beamspace yielding linescan plots similar to that shown in Fig. 10. The 19 overlaid orthogonal beams are shown in Fig. 14. Since the far-field source was held stationary for the purpose of this test, the power roll-off seen in the figure is exclusively a result of the optical scan loss incurred for

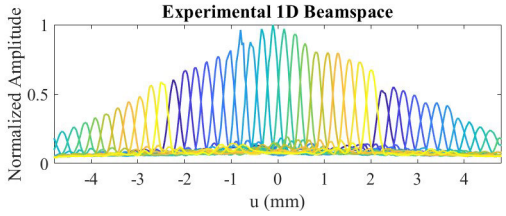

FIGURE 14. Experimentally gathered 1D beamspace generated by phasing RF front end. Discontinuities in color order from yellow to blue signify extent of beamspace array and beginning of grating lobes. Compare experimental result with Fig. 10.

edge beams in the optical processor. The edge beams have approximately 60% of the power contained in the center beam; this is due to a combination of the optical element factor coming into play as well as the increased power of the grating lobe as it reaches the boundary of the beamspace array. We note that this roll-off is in rough agreement with the modeled one-dimensional beamspace shown in Fig. 10; in the simulated example it is expected that the edge beams have roughly 70% of the power of the main beam. Deviations in the construction of the system from ideal, such as sideband amplitude imbalances and errors in the calibration of the system [24], contribute to this discrepancy. However, scan loss on the order of 3 dB for the edge cases represents an improvement over a two-dimensional beamforming network [26] in which a 6-dB penalty is incurred for incidence at the edge of the field-of-view in both azimuth and elevation.

A measure of the planar beamforming capability is highlighted through the preservation of beam orthogonality. Beams manifested by sampled phases across the array agreeing with (10) are maximally distinct as discussed in Sec. III. This relationship is preserved through the transition to a planar beamformer; Fig. 15 illustrates the preservation of two-dimensional orthogonality in the one-dimensional beamspace.

Finally, to demonstrate true planar beamforming for two-dimensional RF scenes, we present two source distributions, with the first following the simulated triple-incidence case shown in Fig. 9. The two source distributions and their corresponding line spread functions are shown in Fig. 16. Since the sources fall into the orthogonal bins, they are maximally distinct, with each maximum lobe falling in the nulls of all unlike beams. Note in Fig. 16 good agreement between the experimental and simulated results—the locations of respective beams are in the positions predicted by the model. The additional loss incurred by the non-broadside beams ($n \neq 0$) in the experiment over the simulation may be explained by the incorporation of RF array scan loss as well as mismatched cable loss not factored into the simulated figures shown at the bottom of Fig. 16, and by the previously mentioned nonidealities in system construction. However, as discussed previously in this Section, when RF scan loss has been isolated, the constructed system shows good agreement with expected performance: Beam 0 in the middle of both the one- and two-dimensional beamspaces

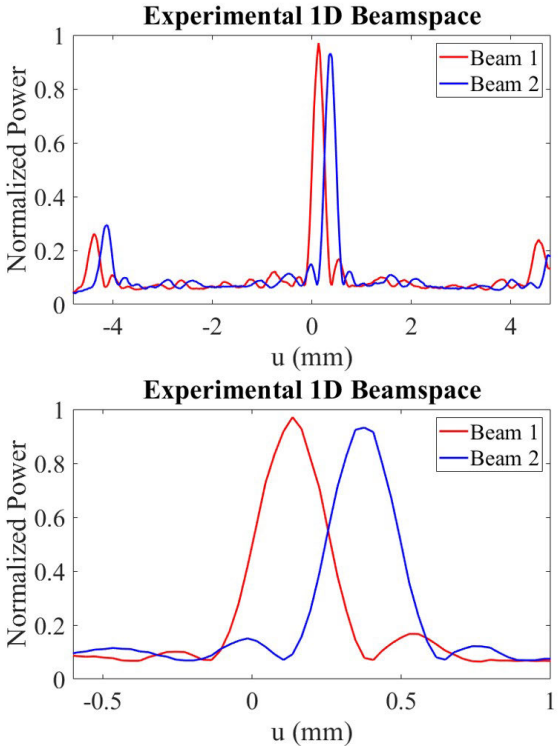

FIGURE 15. Illustration of preservation of orthogonality in 1D Fourier transform. Beam 1 falls in null of Beam 2 and vice versa; this is true for all unlike beams.

has the strongest power; Beams 3 and 14, close to the center, experience diminished scan loss; and Beams 6 and 9, at the edges of the two-dimensional FOV, experience the greatest (but similar) scan loss, as a function of power relative to Beam 0, roughly constant in both cases.

D. VIDEO DEMONSTRATIONS

Video demonstrations of the two-dimensional beamforming capability of the system are included with this manuscript. These videos demonstrate the linear translation of a single source along cardinal axes in the beamspace, steering in the 0-2, 0-3, and 0-5 directions according to the beam enumerations of Fig 6. Further demonstrated is the incidence of three sources at the same time, with each source obstructed in turn to emphasize the contribution of each to the linescan function sampled by the system. The power incident in each bin has been integrated and applied to a color map in which blue represents the weakest contribution, with increasing power resulting in the color changing from blue towards green and yellow and finally white for a saturated bin. The two-dimensional beamspace is reconstructed in real-time by a LabVIEW program with the beamspace enumeration relating the one- and two-dimensional beamspaces included for reference.

VI. DISCUSSION

Beyond harnessing the advantages of planar processing for two-dimensional beamforming, the approach discussed

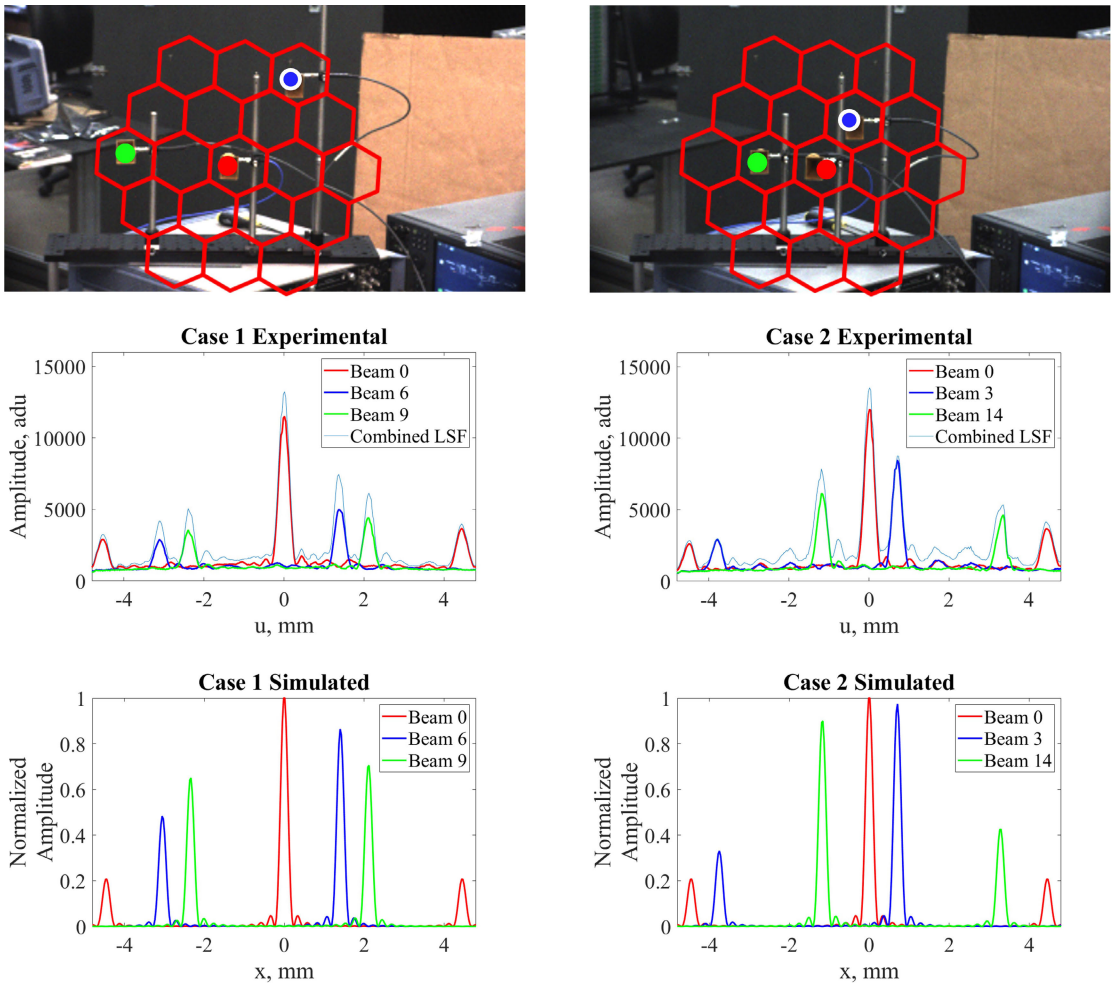

FIGURE 16. Two examples of two-dimensional RF beamforming based on planar optical processing. Three orthogonal beams distributed along two dimensions are imaged with 1D Fourier transforms. Colors overlaid upon sources in upper image correspond to linescan color. Compare experimental result in middle row to simulated result with identical source distribution in bottom row.

herein carries the additional benefit of reducing scan loss for edge beams: the optical scan loss is on the order of 3 dB when moving from the on-axis beam to edge beams. However, if the beamforming process was carried out in two dimensions, moving to the edge in both horizontal and vertical directions would carry a penalty of 6 dB as scan loss would be incurred twice. The focusing of energy in the direction orthogonal to that along which the Fourier transform is taken has been shown to significantly improve the power throughput of the free-space optical processor; simulated studies in which the element-space beam waist was allowed optimization independent of pickup beam waist showed an improvement of on-axis coupling from 38% to 44% and off-axis coupling from 15% to 32%, in line with estimates regarding scan loss [23].

The capability of a planar optical circuit to perform two-dimensional beamforming allows for the use of photonic integrated circuits (PICs) to perform two-dimensional beamspace processing. The free-space optical processor employed in this work consists of a system of lenses placed upon an optical table with a footprint of approximately 0.25 square meters; this represents a three-quarters footprint reduction from the original configuration with a footprint of one square meter [22]. Equivalent PICs containing modulators and photodetectors for phase locking as well as a star coupler or free propagation region (FPR) are typically on the order of 25 square millimeters; in comparison to the free-space processor this represents a footprint reduction of 10,000 times for the beamspace processor. In addition, large-scale production of an application-specific PIC may enable considerable reduction in fabrication cost: the alignment of an optical processor is an arduous and lengthy process while PICs are manufactured to specification. Harnessing the rapidly expanding field of photonic integrated circuits offers potentially unprecedented advances in operational capabilities.

In addition to the extreme reductions in cost, size, weight and power (C-SWAP) requirements associated with moving to planar processing, this approach may be combined with recent sensing paradigms, in which the mmW imaging

modality has additionally incorporated a fiber arrayed waveguide grating (FAWG) for hyperspectral direction-finding [11]. By better tuning a filtering algorithm [27] or tunable optical local oscillator [28] to source characteristics with respect to angle-of-arrival and carrier frequency, adaptive beamforming may be accomplished through complex weighting of the RF front end by way of variable optical attenuators and the same phase modulators enabling coherent up-conversion [29], [30]. Such an approach may provide improvements over prior coherent data recovery experiments [31], [32] using the photonic beamforming approach. With the move to planar optical circuitry, matched filters or other diffractive optical elements may also be incorporated on a case-specific basis to enable further RF scene filtering or signal processing. In short, the benefits associated with the two-dimensional photonic approach remain valid in the planar configuration, while the transformation into one-dimensional element and beamspace arrays positions the technology well to take full advantage of the exploding field of photonic integrated circuits.

While the presented technique carries benefits, such as the potential for analog beamforming on a PIC, it should be noted that for large numbers of channels a PIC becomes impractical. Phased arrays with over $\sim$1000 elements may require some form of subarraying to reduce the input element count to a number of fibers for which it is feasible to construct linear fiber arrays for; at a 250-μm pitch a 1000-element array would require a PIC 250 mm long. With the industry convergent upon 300-mm wafers for large-scale fabrication, such a device would be an extraordinary test of modern fabrication capability.

In sum, the AB mapping approach represents a novel addition to the myriad techniques used in modern phased-array antenna design, a space in which system construction is ultimately informed by the constraints of the intended application.

VII. CONCLUSION

In this work, we present an example of AB Mapping, a method for processing a two-dimensional RF beamspace with a one-dimensional optical Fourier transform in which all RF-scene information is preserved in both up-conversion and reshaping of the element space. The approach is validated with a 19-element hexagonally-spaced RF front end feeding a free-space optical processor employing cylindrical lenses to process and shape the Fourier transform. We believe this technique positions the mmW photonic approach to move from discrete optics deployed upon optical tables to photonic integrated circuits with additional benefits to throughput and enabling further, more in-depth beamspace processing [33], [34], [35].

ACKNOWLEDGMENT

The author William L. Beardell was with the Department of Electrical and Computer Engineering, University of Delaware, Newark, DE, USA.

REFERENCES

[1] C. Balanis, *Antenna Theory: Analysis and Design*, 4th ed. Hoboken, NJ, USA: Wiley, 2016.
[2] D. H. Johnson and D. E. Dudgeon, *Array Signal Processing: Concepts and Techniques* (Signal Processing Series). Englewood Cliffs, NJ, USA: Prentice-Hall, 1993.
[3] J. Huang, C. Liu, W. Hu, and K. Liao, "Design of a grating lobes-free architecture for distributed sensor system with arbitrary element spacing," *Remote Sens.*, vol. 14, no. 6, p. 1356, Mar. 2022. [Online]. Available: https://www.mdpi.com/2072-4292/14/6/1356
[4] C. L. Dolph, "A current distribution for broadside arrays which optimizes the relationship between beam width and side-lobe level," *Proc. IRE*, vol. 34, no. 6, pp. 335–348, Jun. 1946.
[5] A. Safaai-Jazi, "A new formulation for the design of Chebyshev arrays," *IEEE Trans. Antennas Propag.*, vol. 42, no. 3, pp. 439–443, Mar. 1994.
[6] C. J. Ryan, W. L. Beardell, J. Murakowski, D. D. Ross, G. J. Schneider, and D. W. Prather, "Log-periodic temporal apertures for grating lobe suppression in k-space tomography," *Opt. Exp.*, vol. 28, no. 11, p. 15969, May 2020. [Online]. Available: https://www.osapublishing.org/oe/abstract.cfm?doi=10.1364/OE.392118
[7] A. S. Petrov, R. Y. Malakhov, and V. D. Teplyakov, "Specific features of multibeam directional patterns in analog-digitial active phased antenna arrays," *J. Commun. Technol. Electron.*, vol. 64, no. 4, pp. 366–374, Apr. 2019. [Online]. Available: http://link.springer.com/10.1134/S1064226919040077
[8] S. P. Skobelev, "On the forming of orthogonal beams by planar array antennas," *IEEE Trans. Antennas Propag.*, vol. 62, no. 4, pp. 1762–1768, Apr. 2014.
[9] D. A. B. Miller, "Communicating with waves between volumes: Evaluating orthogonal spatial channels and limits on coupling strengths," *Appl. Opt.*, vol. 39, no. 11, p. 1681, Apr. 2000. [Online]. Available: https://opg.optica.org/abstract.cfm?URI=ao-39-11-1681
[10] D. D. Ross, C. J. Ryan, G. J. Schneider, J. Murakowski, and D. W. Prather, "Passive three-dimensional spatial–spectral analysis based on k-space tomography," *IEEE Photon. Technol. Lett.*, vol. 30, no. 9, pp. 817–820, May 1, 2018. [Online]. Available: https://ieeexplore.ieee.org/document/8320802/
[11] C. J. Ryan, W. L. Beardell, J. Murakowski, G. J. Schneider, and D. W. Prather, "Instantaneous microwave-photonic spatial–spectral channelization via k-space imaging," *Opt. Exp.*, vol. 29, no. 13, p. 19928, Jun. 2021. [Online]. Available: https://www.osapublishing.org/abstract.cfm?URI=oe-29-13-19928
[12] T. E. Dillon, C. A. Schuetz, D. G. Mackrides, A. Wright, K. Shreve, C. Harrity, S. Kocazik, S. Shi, P. Yao, and D. W. Prather, "High fill factor RF aperture arrays for improved passive, real-time millimeter wave imaging," *Proc. SPIE*, vol. 10642, pp. 269–277, May 2018. [Online]. Available: https://www.spiedigitallibrary.org/conference-proceedings-of-spie/10642/106420U/High-fill-factor-RF-aperture-arrays-for-improved-passive-real/.full
[13] G. J. Foschini, "Layered space-time architecture for wireless communication in a fading environment when using multi-element antennas," *Bell Labs Tech. J.*, vol. 1, no. 2, pp. 41–59, Aut. 1996.
[14] J. Benesty, Y. Huang, and J. Chen, "A fast recursive algorithm for optimum sequential signal detection in a BLAST system," *IEEE Trans. Signal Process.*, vol. 51, no. 7, pp. 1722–1730, Jul. 2003.
[15] D. G. Mackrides, C. A. Schuetz, R. D. Martin, T. E. Dillon, P. Yao, and D. W. Prather, "Progress toward a video-rate, passive millimeter-wave imager for brownout mitigation," *Proc. SPIE*, vol. 8022, May 2011, Art. no. 802203. [Online]. Available: http://proceedings.spiedigitallibrary.org/proceeding.aspx?doi=10.1117/12.884164
[16] R. D. Martin, S. Shi, Y. Zhang, A. Wright, P. Yao, K. P. Shreve, C. A. Schuetz, T. E. Dillon, D. G. Mackrides, C. E. Harrity, and D. W. Prather, "Video rate passive millimeter-wave imager utilizing optical upconversion with improved size, weight, and power," *Proc. SPIE*, vol. 9462, May 2015, Art. no. 946209. [Online]. Available: https://www.spiedigitallibrary.org/conference-proceedings-of-spie/9462/946209/Video-rate-passive-millimeter-wave-imager-utilizing-optical-upconversion-with/10.1117/12.2177133.short
[17] J. A. Murakowski, G. Schneider, and D. W. Prather, "Optical processing for phased-array and beamspace mapping," *Proc. SPIE*, vol. 12000, pp. 84–89, Mar. 2022. [Online]. Available: https://www.spiedigitallibrary.org/conference-proceedings-of-spie/12000/2613480/Optical-processing-for-phased-array-and-beamspace-mapping/10.1117/12.2613480.full

[18] J. E. Bowers, T. Komljenovic, M. Davenport, J. Hulme, A. Y. Liu, C. T. Santis, A. Spott, S. Srinivasan, E. J. Stanton, and C. Zhang, "Recent advances in silicon photonic integrated circuits," *Proc. SPIE*, vol. 9774, Feb. 2016, Art. no. 977402. [Online]. Available: http://proceedings.spiedigitallibrary.org/proceeding.aspx?doi=10.1117/12.2221943
[19] J. Murakowski, G. Schneider, and D. Prather, "Orthogonal-beam forming by phased arrays," to be published.
[20] R. D. Martin, C. A. Schuetz, D. W. Prather, and T. E. Dillon, "Controlling the phase of optical carriers," Patent 8 159 737, Apr. 8, 2012. [Online]. Available: http://patft.uspto.gov/netacgi/nph-Parser?Sect1=PTO2&Sect2=HITOFF&p=1&u=%2Fnetahtml%2FPTO%2Fsearch-bool.html&r=18&f=G&l=50&co1=AND&d=PTXT&s1=%22phase+sensitive+innovations%22&OS=%22phase+sensitive+innovations%22&RS=%22phase+sensitive+innovations%22
[21] J. W. Goodman, *Introduction to Fourier Optics*, 4th ed. New York, NY, USA: WH Freeman, 2017.
[22] T. E. Dillon, C. A. Schuetz, R. D. Martin, E. L. Stein Jr., J. P. Samluk, D. G. Mackrides, M. S. Mirotznik, and D. W. Prather, "Optical configuration of an upconverted millimeter-wave distributed aperture imaging system," *Proc. SPIE*, vol. 7485, Sep. 2009, Art. no. 74850G. [Online]. Available: http://proceedings.spiedigitallibrary.org/proceeding.aspx?doi=10.1117/12.830493
[23] W. L. Beardell, "Coherent optical processors," M.S. thesis, Dept. Elect. Comput. Eng., College Eng., Univ. Delaware, Newark, DE, USA, 2020.
[24] W. L. Beardell, "Spatial–spectral imaging with microwave photonic arrays," Ph.D. dissertation, Dept. Elect. Comput. Eng., College Eng., Univ. Delaware, Newark, DE, USA, 2022.
[25] R. C. Hansen, *Phased Array Antennas* (Wiley Series in Microwave and Optical Engineering), 2nd ed. Hoboken, NJ, USA: Wiley, 2009.
[26] H. Schrank and K. Praba, "Optimal aperture for maximum edge-of-coverage (EOC) directivity," *IEEE Antennas Propag. Mag.*, vol. 36, no. 3, pp. 72–74, Jun. 1994.
[27] J. N. Mait, "Millimeter wave imaging with engineered point spread functions," *Opt. Eng.*, vol. 51, no. 9, May 2012, Art. no. 091606. [Online]. Available: https://www.spiedigitallibrary.org/journals/optical-engineering/volume-51/issue-9/091606/Millimeter-wave-imaging-with-engineered-point-spread-functions/10.1117/1.OE.51.9.091606.short
[28] G. J. Schneider, J. A. Murakowski, C. A. Schuetz, S. Shi, and D. W. Prather, "Radiofrequency signal-generation system with over seven octaves of continuous tuning," *Nature Photon.*, vol. 7, no. 2, pp. 118–122, Feb. 2013. [Online]. Available: http://www.nature.com/articles/nphoton.2012.339
[29] A. R. Margetts, E. G. Torkildson, R. Bartlett, and S. Kraut, "Optimal training and data power allocation for distributed transmit beamforming," in *Proc. Asilomar Conf. Signals, Syst. Comput.*, Nov. 2013, pp. 587–591.
[30] C. Hayes, A. R. Margetts, C. Martin, H. Nguyen, W. Song, and J. Muldavin, "Informed MIMO implementation of distributed transmit beamforming for range extension," in *Proc. IEEE Radio Wireless Symp. (RWS)*, Jan. 2016, pp. 256–258.
[31] J. C. Deroba, G. J. Schneider, C. A. Schuetz, and D. W. Prather, "Multifunction radio frequency photonic array with beam-space down-converting receiver," *IEEE Trans. Aerosp. Electron. Syst.*, vol. 54, no. 6, pp. 2746–2761, Dec. 2018.
[32] W. Beardell, B. Mazur, C. Ryan, G. Schneider, J. Murakowski, and D. Prather, "RF-photonic spatial–spectral channelizing receiver," *J. Lightw. Technol.*, vol. 40, no. 2, pp. 432–441, Jan. 15, 2022.
[33] R. Menon, "Resurgence of diffractive optics in imaging, sensing, and inferencing," *Proc. SPIE*, vol. PC12011, Mar. 2022, Art. no. PC120110P. [Online]. Available: https://www.spiedigitallibrary.org/conference-proceedings-of-spie/PC12011/PC120110P/Resurgence-of-diffractive-optics-in-imaging-sensing-and-inferencing/10.1117/12.2614056.full
[34] D. R. Solli and B. Jalali, "Analog optical computing," *Nature Photon.*, vol. 9, no. 11, pp. 704–706, Nov. 2015. [Online]. Available: https://www.nature.com/articles/nphoton.2015.208
[35] G. Zheng, H. Mühlenbernd, M. Kenney, G. Li, T. Zentgraf, and S. Zhang, "Metasurface holograms reaching 80% efficiency," *Nature Nanotechnol.*, vol. 10, no. 4, pp. 308–312, Apr. 2015. [Online]. Available: https://www.nature.com/articles/nnano.2015.2

WILLIAM L. BEARDELL (Student Member, IEEE) received the B.S., M.S., and Ph.D. degrees from the University of Delaware, Newark, DE, USA, in 2018, 2020, and 2022, respectively, with a research focus on spatial-spectral beamforming techniques with microwave photonic arrays.

He is currently a member of the Senior Professional Staff with The Johns Hopkins University Applied Physics Laboratory. His research interests include integrated photonics and phased-array radar.

JANUSZ MURAKOWSKI received the M.S. degree in physics from Adam Mickiewicz University, Poznan, Poland, in 1990, the M.S. degree in physics from Imperial College London, London, U.K., in 1991, and the Ph.D. degree in physics from the University of Delaware, USA, in 1999. Until 2022, he was an Associate Research Professor with the Department of Electrical and Computer Engineering, University of Delaware. He currently holds the position of a Senior Scientist with Phase Sensitive Innovations Inc., Newark, DE, USA. He is the author or coauthor of several books and book chapters, and more than 100 peer-reviewed journal and conference publications. He holds 31 issued U.S. patents. His areas of expertise include electromagnetic science and engineering, micro- and nano-fabrication, as well as photonic and electro-optic system design and innovation in addition to photonic modeling, design, fabrication, and characterization. His research interests include RF/microwave photonics, including system design, electro-optic modulation, nonlinear optical processes, transmission, detection, and imaging.

GARRETT J. SCHNEIDER received the B.S. degree in astronomy and physics from the Haverford College, Haverford, PA, USA, in 1993, and the Ph.D. degree in physics from the University of Delaware, Newark, DE, USA, in 2002.

Since 2002, he has been with the Department of Electrical and Computer Engineering, University of Delaware, where he is currently an Assistant Research Professor. He is also a Consulting Engineer with Phase Sensitive Innovations Inc., Newark. He is the coauthor of more than 100 peer-reviewed journals and conference publications, as well as several books/book chapters, and has 12 issued patents in the fields of nanofabrication and RF photonic system design. His areas of expertise include nonlinear optics, microwave photonics, optical and RF device and system characterization techniques, and nanofabrication. His current research interests include RF/microwave/millimeter-wave photonics for applications in telecommunications and remote sensing.

DENNIS W. PRATHER (Fellow, IEEE) received the B.S.E.E., M.S.E.E., and Ph.D. degrees from the University of Maryland, College Park, MD, USA, in 1989, 1993, and 1997, respectively.

He is currently the College of Engineering Distinguished Professor with the Department of Electrical and Computer Engineering, University of Delaware, Newark, DE, USA, where he established the Laboratory for RF and Integrated-Photonic Systems. He has authored or coauthored more than 500 scientific articles, holds more than 35 patents, and has written 14 books/book-chapters. He is a fellow of the Optical Society of America, the Society of Photo-Instrumentation Engineers, and the National Academy of Inventors.